EFDA–JET–PR(09)27

M. Gelfusa, A. Murari, P. Gaudio, A. Boboc, M. Brombin, F.P. Orsitto,
E. Giovannozzi and JET EFDA contributors

A New Calibration Code for the JET Polarimeter

A New Calibration Code for the JET Polarimeter

M. Gelfusa[1], A. Murari[2], P. Gaudio[1], A. Boboc[3], M. Brombin[2], F.P. Orsitto[4], E. Giovannozzi[4] and JET EFDA contributors*

JET-EFDA, Culham Science Centre, OX14 3DB, Abingdon, UK

[1] Associazione EURATOM-ENEA - University of Rome "Tor Vergata" , Roma, Italy
[2]Consorzio RFX Associazione EURATOM-ENEA per la Fusione, 4-35127 Padova, Italy
[3]EURATOM-CCFE Fusion Association, Culham Science Centre, OX14 3DB, Abingdon, OXON, UK
[4]Associazione EURATOM-ENEA – CR Frascati 00044 Frascati, Italy
** See annex of F. Romanelli et al, "Overview of JET Results",*
(Proc. 22 [nd] IAEA Fusion Energy Conference, Geneva, Switzerland (2008)).

Preprint of Paper to be submitted for publication in
Review of Scientific Instruments

ABSTRACT.
A complete model of JET Polarimeter is presented, which overcomes the drawbacks of previous version of the fitting procedures used to provide calibrated results. First of all the signal processing electronics has been simulated, to confirm that it is still working within the original specifications.Then the effective optical path of both the vertical and lateral chord has been implemented to produce the calibration curves. The principle approach to the model has allowed obtaining a unique procedure which can be applied to any manual calibration and remains constant until the following one. The optical model of the chords is then applied to derive the plasma measurements. The results are in good agreement with the estimates of the most advanced full wave propagation code available and have been benchmarked with other diagnostics. The devised procedure has proved to work properly also for the most recent campaigns and the high current experiments.

1. INTRODUCTION

Thermonuclear plasmas are active and anisotropic media, which strongly affect the propagation of electromagnetic radiation, depending on their parameters. The measurement of the change in the polarization state (Faraday rotation and Cotton-Mouton effect) of a laser beam probing a plasma can therefore provide very useful information about various physical quantities crucial for both the understanding of the physics and the control of the configuration. As a consequence, polarimetric diagnostics have become quite common in experiments studying nuclear fusion plasmas, particularly because they provide very useful information about various physical quantities crucial for both the understanding of the physics and the control of the configuration. Typically in polarimetry a linearly polarised laser beam probes the plasma and its polarisation output is compared with the initial one.

On JET, a dual interferometer/polarimeter system carries out, routinely, the Faraday rotation and Cotton-Mouton effect measurements. On JET these measurements are complicated by two facts: first the general issue of the nonlinear interaction between the Faraday rotation and the Cotton Mouton effect and second a "spurious" phase shift induced by non identified optical components of the diagnostic. The effect of this spurious instrumental phase shift must be taken into account in the calibration and signal processing procedures.

Since, the optical components introducing the spurious effects are completely unknown, then the previous calibration procedure has been based on an empirical model in which purely numerical and quite complex fitting procedures are implemented to evaluate the calibration parameters and the polarimetric measurements. This processing method has been developed without any investigation on the source of the spurious effect and it works as a black box without a clear relation with the hardware setup. A statistical analysis, carried out on the polarimetric measurements acquired during the campaigns 2003-2009, has highlighted some calibration problems affecting mainly the experimental data of the most recent campaigns (2008-2009) particularly those of the high current discharges. Therefore, it has been decided to develop a new calibration code, based on the layout and therefore on the physics of the diagnostic.

This new calibration code is based on the description of propagation of laser beam through all optical components of the polarimetry system. To this end the well-known Mueller matrix formalism [1] has been used.

The paper is organized as follows: in section 2, after a brief description of JET interferometer/ polarimeter system, a virtual simulator developed to verify the correct operation of the signal processing electronics is presented; in sections 3 the new calibration code for the vertical and the lateral chords is described and in the last section the first results obtained are shown.

2. JET INTERFEROMETER/POLARIMETER

2.1. POLARIMETRIC MEASUREMENTS

Two separate phenomena influence the polarisation of the Far InfraRed (FIR) beam that passes through a magnetically confined plasma [4]:

• **Faraday Rotation effect**: the plane of linearly polarised light passing through a plasma is rotated when a magnetic field is applied parallel to the direction of propagation according to the relation

$$\Delta\Psi \propto \lambda^2 \int n_e \cdot B_{\mathrm{II}} \cdot dz \tag{1}$$

• **Cotton-Mouton effect**: the ellipticity acquired by a linearly polarised light passing through a plasma is dependent on the density and the magnetic field perpendicular to the direction of propagation.

$$\Phi \propto \lambda^3 \int n_e \cdot B_{\perp}^2 \cdot dz \tag{2}$$

Here λ is the laser wavelength, n_e is the plasma electron density and B_{II} and $B_{\perp}$ the parallel and perpendicular components of the magnetic field respectively. After traversing the plasma a polarised beam suffers a rotation of the polarisation plane due to Faraday Rotation and acquires ellipticity due to the Cotton-Mouton effect.

2.2. DESCRIPTION OF THE DIAGNOSTIC

At JET, the Far InfraRed diagnostic operates as a dual interferometer/polarimeter system.

The system consists of 4 vertical and 4 lateral laser beams which provide measurements of the lineintegrated plasma density by means of interferometry and Faraday Rotation angle and Cotton-Mouton effect by polarimetry [2, 3].

The radiation, provided by a DCN laser at 195μm, is split into a probing beam and a reference beam , which is modulated by a rotating wheel at 100kHz.

After the vessel, the probing and the reference beam are recombined (with a recombination quartz plate) and then they reach a wire grid which divides the electric field components into two orthogonal directions, that are focused onto two InSb He-cooled detectors.

The layout of the system, for one vertical chord, is shown in figure 1.

The Faraday rotation angle is measured on all 8 channels by evaluating the two components of polarisation of the laser beam that passes through the plasma. These measurements are receded by an on-line calibration performed before each shot (using half-wave plates) [2, 3]. In order to measure the Cotton-Mouton angle, a special set-up, with initial linear polarisation of the input beam set at 45 degrees with respect to the toroidal field direction (x-axis) for the vertical channels and parallel to the toroidal field for the horizontal channels, has been implemented.

The grid and half-wave plate before the entrance window are used to set the required direction of the linear input polarisation. In the calibration phase this half-wave plate is rotated before each discharge to simulate the Faraday rotation effect.

The amplitudes of the measured beat signals are proportional to the orthogonal components of the corresponding electric field vector amplitudes of the electromagnetic wave in the local co-ordinate system [3] defined by the orientation of the wire grid in front of the detectors:

$$p(t) \propto E_y \cos(\omega_0 t - \varphi) = E_y^0 \sin\Theta \cdot \cos(\omega_0 t - \varphi) \tag{3}$$

$$i(t) \propto E_x \cos(\omega_0 t) = E_x^0 \cos\Theta \cdot \cos(\omega_0 t) \tag{4}$$

where ω_0 is the modulation frequency (100 kHz) obtained by a rotating grating wheel, φ is the phase shift between the orthogonal components, E_x and E_y are the components of the electrical vector, and $\Theta = \Theta_0 + \alpha$ with $\Theta_0 = 45^{\circ}$. In presence of plasma α represents the Faraday angle; during the calibration it is equal to twice the rotation angle of the half-wave plate.

The amplified signals are sent to a phase sensitive electronic module to produce four additional signals that are sent to the data acquisition system.

2.3. SIGNAL PROCESSING ELECTRONICS

The present electronics used to process data from the detectors of the JET Far Infrared polarimeter has been commissioned in 2002. Since in the last years the diagnostic has been configured for measuring routinely both the Faraday Rotation effect and the Cotton-Mouton effect with a different optical set-up, it becomes important to check the performance of the analog phase sensitive electronics [3].

The main operation performed by the analog electronics of the polarimeter have been implemented via software using both Simulink and Matlab. This allows an accurate characterisation of the instrument and an assessment of the quality of the provided measurements. The detected signals (*i(t)* and *p(t)*) are processed via analog phase sensitive electronics to obtain the following measurements: *RMS*, *RMP*, *PSP* and *PSD*:

$$RMS = \langle i(t) \times i(t) \rangle \tag{5}$$

$$RMP = \left\langle i'(t) \times i'(t) \right\rangle \tag{6}$$

$$PSD = \left\langle i(t) \times p(t) \right\rangle \tag{7}$$

$$PSP = \left\langle i'(t) \times p(t) \right\rangle \tag{8}$$

where $i'(t) \propto \sin(w_0 t)$ is generated by shifting of 90 degrees the phase of the *i(t)* signal.

These four signal are processed by a code to obtain the two ratios R and R′ which are related to polarimetric parameters of the radiation after the plasma:

$$R = \frac{PSD}{RMS} = C^{-1} \tan(\Theta) \cdot \cos\varphi \tag{9}$$

$$R' = \frac{PSP}{\sqrt{RMS \cdot RMP}} = C^{-1} \tan(\Theta) \cdot \sin\varphi \tag{10}$$

where *C* is a calibration factor.

Given the two ratio R and R′, the main parameters of the electrical vector of the polarised radiation can be derived:

- the phase shift

$$\varphi = arctg\frac{R'}{R} = \phi_0 + \Phi \tag{11}$$

  where ϕ_0 is the phase shift between the two signals in absence of plasma, while Φ represents the angle introduced by the Cotton-Mouton effect.
- the ratio Θ between the orthogonal components of the electrical vector

$$R^2 + R'^2 = C^{-2} \tan^2\Theta \Rightarrow \tan^2\Theta = C^2\left(R^2 + R'^2\right) \tag{12}$$

The optical properties of the polarised light, polarisation angle (ψ) and ellipticity ($\varepsilon = \tan\chi$) can be derived using the well known identities which relate the electrical parameters to the geometrical ones:

$$\tan(2\psi) = \tan(2\Theta)\cos\varphi \tag{13}$$

$$\sin(2\chi) = \sin(2\Theta)\sin\varphi \tag{14}$$

The parameter ψ is the polarisation angle between the major axis of the polarisation ellipse (see figure 2) and the reference x-axis; the parameter χ is related to the ellipticity of the radiation.

2.3.1 Electronics bench test: hardware set-up and data processing

The tests to check the reliability of the electronic cards used on polarimetry have mainly consisted on acquiring the raw data after the detectors, process them via software and then compare the obtained outputs with the ones given by from the polarimeter electronics. The first test has been performed getting the raw signals after the band pass filter (80 – 120 kHz) before the phase analog sensitive detector (see figure 1). Then the data have been processed by an electronic simulator realised by Simulik software. For the second and more recent test the data have been taken after the detectors, before the band pass filter. This second set of signals has been analysed with a Matlab code, which implements the band pass filter and the main operations of the phase sensitive detector (eq 5 - 8).

Looking to figure 3 it is clear the good agreement between the simulated signals and the real ones provided by the electronics of the polarimeter. This confirms that the phase sensitive detector is still working properly within its design parameters.

3. CALIBRATION PROCEDURE

At JET an on-line calibration, to link the output voltage of the detectors to the effective Faraday rotation angle, is carried out, for each chord, before each shot.

Currently, the procedure of calibration is the following: the half-wave plate, located at the entrance of the vacuum vessel (see figure 1), is rotated (via a step-motor) of a well-known angle (α) and the phase shift (φ) is recorded at each angle, while the Faraday rotation (2α) is equal to twice the halfwave plate angle.

Moreover, before each campaign, or when it is necessary, a manual calibration is performed. It is consist in a rotation of the wire grid, located in front of the two detectors, to optimise the signals revealed.

Figures 4 and 5 show examples of the calibration curves for the vertical chord #3. Figure 4 represents the Faraday angle as function of the time. Figure 5 shows the phase shift vs the half-wave plate rotation.

From figure 5 it is clear that the value of phase shift is not constant when the half-wave angle is varied, as it would be expected for a system with only ideal optical components. Because of this non ideal behaviour, at JET the polarimetric signals are processed using a model which assumes that an unspecified optical element generates a "*spurious ellipticipy*" characterized by a constant phase shift referred to a rotated co-ordinate system of unknown orientation [3].

3.1 NEW CALIBRATION CODE FOR THE VERTICAL CHORDS

As mentioned, a new calibration code has been developed to provide a more robust calibration procedure valid over the whole range of JET discharges.

In the new code all optical components, crossed by the laser beam for the vertical chords, have been modelled using the Mueller Matrix formalism.

Referring to the polarimeter schematic reported in figure 1, the optical components involved in the model are: the half-wave plate and the wire grid located in front of the detectors. A cascade of two retarders is used to reproduce the "*spurious ellipticipy*" which afflicts the polarimetry measurements. The calibration of Faraday angle is carried out rotating the half-wave plate, in absence of plasma, by a known angle (α). So, the Mueller matrix for this component is [8, 9]:

$$M_\alpha = \begin{vmatrix} 1 & 0 & 0 & 0 \\ 0 & \cos 2\alpha & \sin 2\alpha & 0 \\ 0 & -\sin 2\alpha & \cos 2\alpha & 0 \\ 0 & 0 & 0 & 1 \end{vmatrix} \tag{15}$$

that represents the matrix of an ideal rotator. It is primarily used just to change the polarization direction of the beam without modifying the ellipticity.

The two retarders introducing the spurious ellipticity have been modelled with their correspondent Mueller matrices, which in the case of an ideal retarder with a phase shift $(\delta)_1$ and its fast axis along x , is:

$$M_{\delta_1} = \begin{vmatrix} 1 & 0 & 0 & 0 \\ 0 & 1 & 0 & 0 \\ 0 & 0 & \cos\delta_1 & \sin\delta_1 \\ 0 & 0 & -\sin\delta_1 & \cos\delta_1 \end{vmatrix} \tag{16}$$

If the fast axis of the retarder is rotated by an angle α_1 from x , the Muller matrix is:

$$M'_{\delta_1} = R(\alpha_1)\cdot M_{\delta_1}\cdot R(-\alpha_1) \tag{17}$$

where $R(\alpha_1)$ is a rotation matrix.

$$R_{\alpha_1} = \begin{vmatrix} 1 & 0 & 0 & 0 \\ 0 & \cos 2\alpha_1 & \sin 2\alpha_1 & 0 \\ 0 & -\sin 2\alpha_1 & \cos 2\alpha_1 & 0 \\ 0 & 0 & 0 & 1 \end{vmatrix} \tag{18}$$

For the second retarder the Mueller matrix therefore is:

$$M'_{\delta_2} = R(\alpha_2)\cdot M_{\delta_2}\cdot R(-\alpha_2) \tag{19}$$

To estimate the phase shift values (α_2 and α_2) and the angles at which the retarders are located (α_1 and α_2) in the Torus coordinate system, an optimization routine has been written. The routine finds the values of these four quantities which allow to best fit the phase shift curve, shown in figure 5.

The last optical component involved in the calibration code is the wire grid, which acts as an analyser, dividing the electric field components into two directions x and y , which are focused onto the corresponding detectors.

Assuming an ideal behaviour of the analyser, the Mueller matrices for transmission and reflection, M_T and M_R, can be written:

$$M_T = p_x^2 \cdot \begin{vmatrix} p_x^2 + p_y^2 & p_x^2 - p_y^2 & 0 & 0 \\ p_x^2 - p_y^2 & p_x^2 + p_y^2 & 0 & 0 \\ 0 & 0 & 2 \cdot p_x \cdot p_y & 0 \\ 0 & 0 & 0 & 2 \cdot p_x \cdot p_y \end{vmatrix} \tag{20}$$

$$M_R = p_y^2 \cdot \begin{vmatrix} p_x^2 + p_y^2 & p_x^2 - p_y^2 & 0 & 0 \\ p_x^2 - p_y^2 & p_x^2 + p_y^2 & 0 & 0 \\ 0 & 0 & 2 \cdot p_x \cdot p_y & 0 \\ 0 & 0 & 0 & 2 \cdot p_x \cdot p_y \end{vmatrix} \tag{21}$$

where p_x and p_y are, respectively, the cosine and the sine of the wire grid angle.

In ideal conditions, the wire grid should be at 45 degrees with respect to the propagation direction of the radiation, dividing the electric field into the directions x and y.

Looking at the two detector signals, it is possible to estimate the angle between the wires and the incidence electric field of the radiation. As it is shown in figure 5, there is an angle of the polarization for which the phase shift diverges to $\pm\infty$. Since this corresponds to a polarisation for which the R signal equals zero and therefore p(t) signal equals zero, it means that all the radiation is collected by the i(t) detector. This condition is verified when the wires are parallel to the direction of p(t) signal. Then the position of the wire with respect to the incidence electric field can be estimated as:

$$\alpha_{WG2} = 90 - \alpha_0 \tag{22}$$

After this component, the laser beam is divided in two parts and the corresponding Stokes vectors are given by:

$$\vec{S}_{1,R} = M_R \cdot M'_{\delta_2} \cdot M'_{\delta_1} \; M_\alpha \cdot \vec{S}_0 \tag{23}$$

$$\vec{S}_{1,T} = M_T \cdot M'_{\delta_2} \cdot M'_{\delta_1} \cdot M_\alpha \cdot \vec{S}_0 \tag{24}$$

The final Stokes vector ($\vec{S}_1$) is the combination of these two Stokes vectors.

Therefore, it is possible to know the polarisation angle and the phase shift, given by:

$$\psi = \frac{1}{2} arctag\left(\frac{S_2}{S_1}\right) \tag{25}$$

$$\Phi = arctag\left(\frac{S_3}{S_2}\right) \tag{26}$$

where S_1 S_2, and S_3 are the component of the final Stokes vector ($\vec{S}_1$).

These parameters are linked to the Faraday rotation angle (Ψ) and to the Cotton-Mouton effect (Φ):

In the following figures (6-7), the fits of the experimental calibration curves obtained with the new calibration code are reported.

3.2 NEW CALIBRATION CODE FOR THE LATERAL CHORDS

In the following figure the layout of JET Polarimeter for a lateral chord is shown.

From figure 8, it is clear that is not possible to apply directly the new calibration code, developed for the vertical channels, to the horizontal lines of sights because the laser path for the lateral chords is different.

In this case, the radiation passes through the plasma and then it is reflected back using a mirror located on the inner wall. So, in the calibration code this additional optical component has been introduced, which is described by the following Mueller matrix:

$$M_\varepsilon = \begin{vmatrix} 1 & 0 & 0 & 0 \\ 0 & \cos 2\varepsilon & \sin 2\varepsilon & 0 \\ 0 & -\sin 2\varepsilon & \cos 2\varepsilon & 0 \\ 0 & 0 & 0 & 1 \end{vmatrix} \tag{29}$$

that represents the matrix of an ideal rotator. In the case of the polarimeter lateral chords it has been found that the matrix of an ideal mirror, with ε equal to 180 degrees, is more than adequate to obtain satisfactory results.

The other components involved in the model are the same considered for the vertical chords: the half-wave plate, the wire grid located in front of the detectors and the two retarders introduced to reproduce the "*spurious ellipticipy*".

So, for the horizontal chords, the Stokes vectors after the wire grid (WG2) are given by:

$$\vec{S}_{1,R} = M_R \cdot M'_{\delta_2} \cdot M'_{\delta_1} \cdot M_\varepsilon \cdot M_\alpha \cdot \vec{S}_0 \tag{30}$$

$$\vec{S}_{1,T} = M_T \cdot M'_{\delta_2} \cdot M'_{\delta_1} \cdot M_\varepsilon \cdot M_\alpha \cdot \vec{S}_0 \tag{31}$$

where the matrices M_T, $M'_{\delta 2}$, $M'_{\delta 1}$ and $M\alpha$ are the same seen in the previous section.

Since the only difference with respect to the vertical chords is the presence of the mirror, which can be easily modelled with a fixed Mueller matrix, the new calibration procedure and the subsequent elaboration of the raw data, to evaluate the Faraday rotation and the phase shift angle, is the same as for the vertical channels. Again only four quantities (the phase shift values δ_1 and δ_2 and the angles at which the retarders are located α_1 and $\alpha_2 \pm$ in the Torus coordinate system) have to be determined with a series of scans.

4. APPLICATION TO THE PLASMA MEASUREMENTS

Once obtained the calibration curves for the Faraday rotation and the Phase shift, the experimental data have been analyzed applying the new calibration code.

Starting from the raw data acquired, *RMS*, *RMP*, *PSP* and *PSD*, one can obtain the components of Stokes vector [8], which describe the polarisation state of the beam passes through all the optical components and the plasma, using the following equations (see section 2):

$$RMS = \frac{1}{2} E_{H,0}^2 \tag{32}$$

$$RMP = \frac{1}{2} E_{H,0}'^2 \tag{33}$$

$$PSD = \frac{1}{2} E_{H,0}' \cdot E_{V,0} \cos\varphi \tag{34}$$

$$PSP = \frac{1}{2} E_{H,0} \cdot E_{V,0} \cos\varphi \tag{35}$$

where the $E_{H,0}$ and $E_{V,0}$ are the electric field components measured, respectively, with the H-detector and the V-detector (see figure 1) and φ is the phase shift between them.

Since the position of the output wire grid could be rotated with respect to the original reference axes, a rotation of its output components has to be performed to express them in the right coordinate system. To this purpose the electric field components after the wire grid analyser have to be expressed by means of the following transformations:

$$E_x = \alpha \cdot E_{H,0} + \delta \cdot E_{V,0} \tag{36}$$

$$E_y = -\delta \cdot E_{H,0} + \alpha \cdot E_{V,0} \tag{37}$$

where α and δ are, respectively, the cosine and the sine of the wire grid angle in the Torus coordinate system. Once derived the components of the electric field at the exit of the plasma, the final Stokes vector ($\vec{S}_1$) can be calculated [8].

Hence, applying the calibration matrices to $\vec{S}_1$, it is possible to evaluate the plasma effects on the initial polarization state of laser beam, according to:

$$\vec{S}_1 = M'_{\delta_2} \cdot M'_{\delta_1} \cdot M_{\alpha} \cdot M_{Plasma} \ \vec{S}_0 \tag{38}$$

and thus:

$$M_{\alpha}^{-1} \cdot M_{\delta_1}^{-1} \cdot M_{\delta_2}^{-1} \cdot \vec{S}_1 = M_{Plasma} \cdot \vec{S}_0 \tag{39}$$

for the vertical chords, while for the horizontal chords the relation is:

$$M_{\alpha}^{-1} \cdot M_{\varepsilon} \cdot M'^{-1}_{\delta_1} \cdot M'^{-1}_{\delta_2} \cdot \vec{S}_1 = M_{Plasma} \cdot \vec{S}_0 \tag{40}$$

After this procedure, the calibration parameter C, due to the signal processing electronics, is estimated. Since in absence of plasma the Faraday rotation must be equal to twice the half-wave angle, it is easy to find C comparing the experimental data (before 40s) with this curve.

Figure 9 depicts the Faraday rotation calculated with the new calibration code (NewCal), in comparison with the results of a computational model based on the rigorous numerical solution of the Stokes equations [4] (asterisk). Starting from the Lidar Thomson scattering density profiles and the equilibrium magnetic field as input, this code gives as output the Faraday rotation angle and the Cotton Mouton effect for all vertical chords of JET polarimetry [10].

In figure 10 the same comparison for the phase shift is shown. The new calibration is in good agreement with the numerical solution.

Figures 11-22 depict the results obtained for some shots acquired during the 2003-2007 experimental campaigns.

Given the good results obtained for the earlier campaigns, the new calibration code has been applied to the shots performed during 2008-2009 and, also in this case, the comparison between the Stokes model outputs and the new calibration shows a good agreement.

On JET, for the vertical chords, it is easy to evaluate the density from the Cotton-Mouton measurements, because the toroidal field (B_t) is largely constant along the line of sight, and thus equation (2) can be rewritten as:

$$\Phi = k \cdot \lambda^3 \cdot B_t^2 \ \int n_e \cdot dz \tag{41}$$

and therefore the line-integrated electron density (n_e) can be directly obtained:

$$\int n_e \cdot dz = \frac{\Phi}{k \cdot \lambda^3 \cdot B_t^2} \tag{42}$$

where k is a constant.

In the figures 23, 24, 25, the density calculated applying the new calibration code, for the vertical chords, (Density-NC) is reported. The curve is compared with the computational model output (Density-Stokes) and with the density measurement of the interferometer (Interferometer).
As it is clear, using the new calibration the density calculated with the polarimeter and with the interferometer are in good agreement.

CONCLUSIONS

JET polarimeter has been analyzed to understand and to solve the problems posed by the spurious ellipticity induced by the instrument optical components. Two analyses have been perfromed:

1. check of the signal processing electronics to exclude additional anomalous behaviours;
2. development of a new calibration code.

A virtual simulator has been developed to verify the proper operation of the electronics. the analysis shows a very good agreement between the simulation outputs and the experimental data. Therefore, we can conclude that the signal processing electronics is still working within its design parameters.

After this analysis, a new calibration code has been written and tested for many shots acquired in different campaigns. The experimental data, calibrated with this code, has been compared with the rigorous numerical solution of the Stokes equations. The obtained results show that the two estimates are in good agreement for both the Faraday rotation and the Cotton-Mouton effect.

Moreover, starting from the phase shift obtained with this new code, the electron density has been evaluated for the vertical channels and compared with the density measured by the interferometer. the comparison with the experimental measurements confirms the quality of the developed calibration procedure.

ACKNOWLEDGMENTS

This work, supported by the European Communities under the contract of Association between EURATOM and ENEA, was carried out under the framework of the European Fusion Development Agreement. The views and opinions expressed herein do not necessarily reflect those of the European Commission.

REFERENCES:

[1]. D. Goldstein, Polarized Light, CRC Press, 2003.
[2]. K. Guenther, Proceedings of the 31st EPS, P5-172, 2004
[3]. K. Guenther and JET-EFDA Contributors, Plasma Phys. Controlled Fusion **46**, 1423 (2004).
[4]. F. De Marco and S. Segre, Plasma Phys. **14**, 245 (172).
[5]. Cedric Brault CEA, Mission report, March 2009.
[6]. http://www.mathworks.com.
[7]. http://www.tina.com.

[8]. M. Born and E. Wolf, Principles of Optics, Pergamon Press, Oxford, 1980.

[9]. D. S. Kliger, J. W. Lewis, C. E. Randall, Polarized Light in Optics and Spectroscopy, Academic Press, USA, 1990.

[10]. F P Orsitto , A. Boboc, C Mazzotta, E. Giovannozzi, L. Zabeo and JET EFDA Contributors (2008) Plasma Phys Contr Fusion **50** 115009

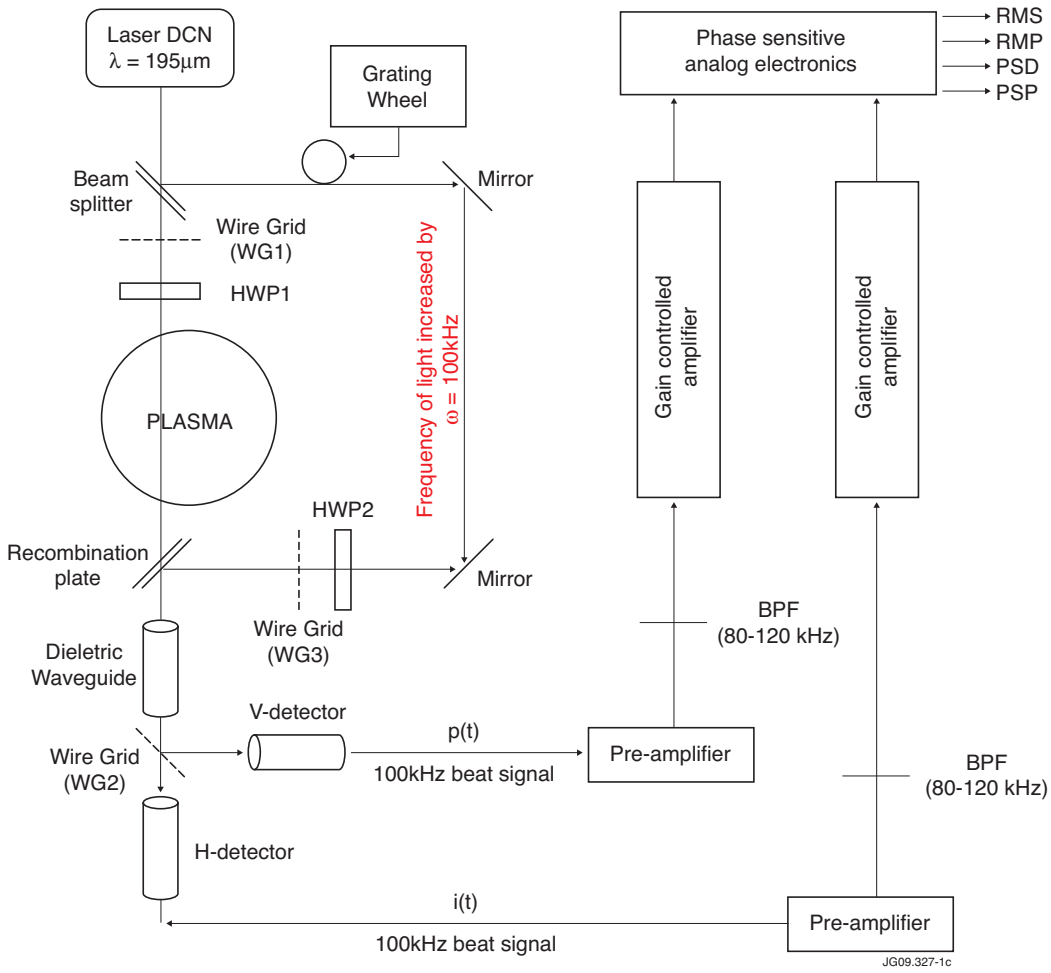

Figure 1: Schematic of the Polarimeter vertical chords.

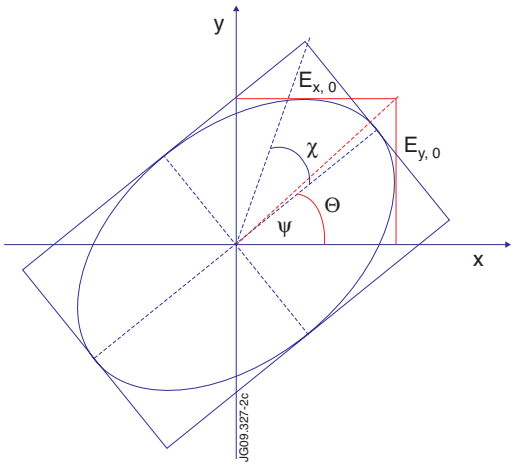

Figure 2: The polarisation ellipse is often adopted to represent the relation between the electrical and the geometrical parameters of the polarised radiation.

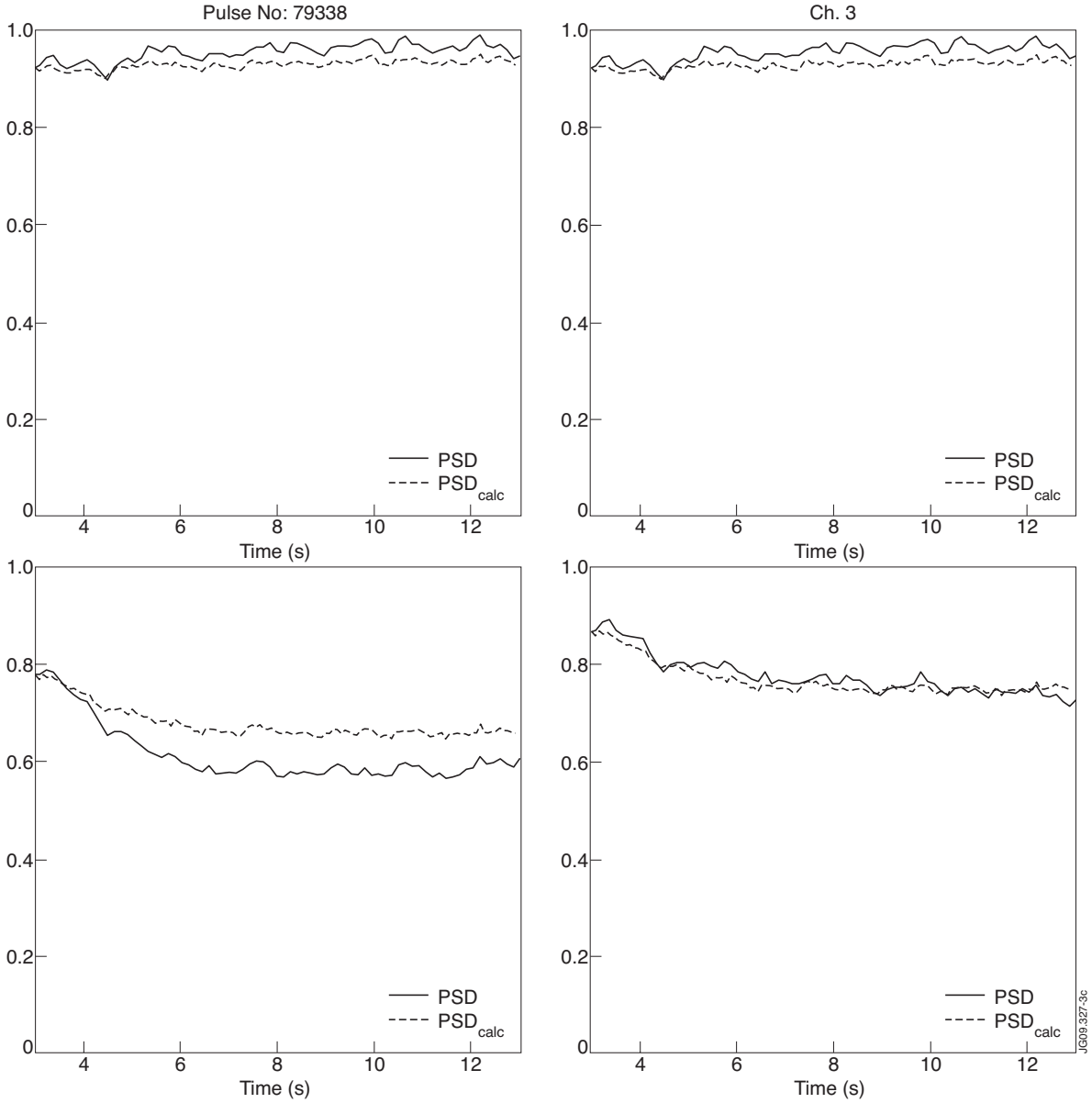

Figure 3:Comparison between the RMS, RMP, PSD, PSP signals coming from polarimetric raw data (continuous line) and from Matlab electronics simulator (dashed line).

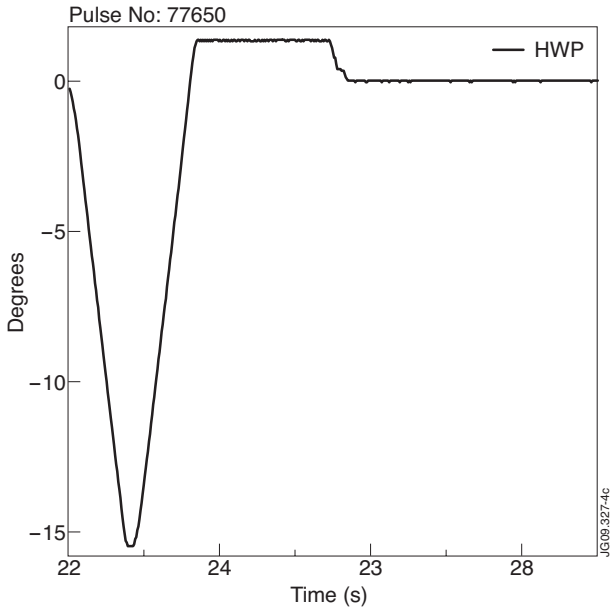

Figure 4: Calibration curve of the Faraday rotation (Pulse No: 77650 chord #3).

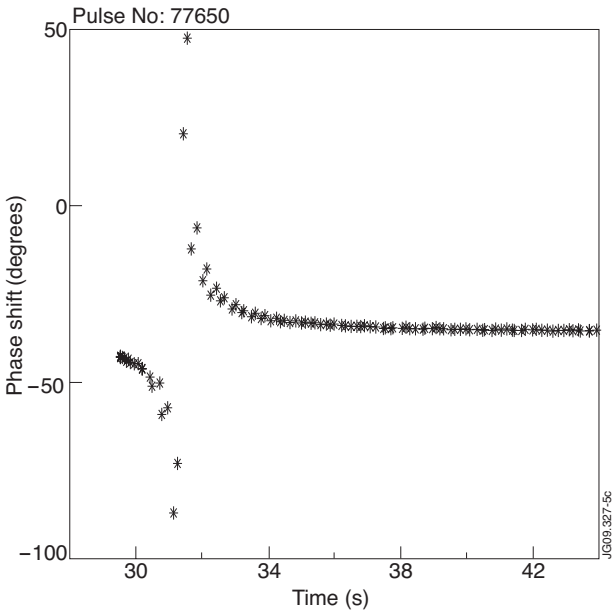

Figure 5: Phase shift calibration curve (Pulse No: 77650 chord #3).

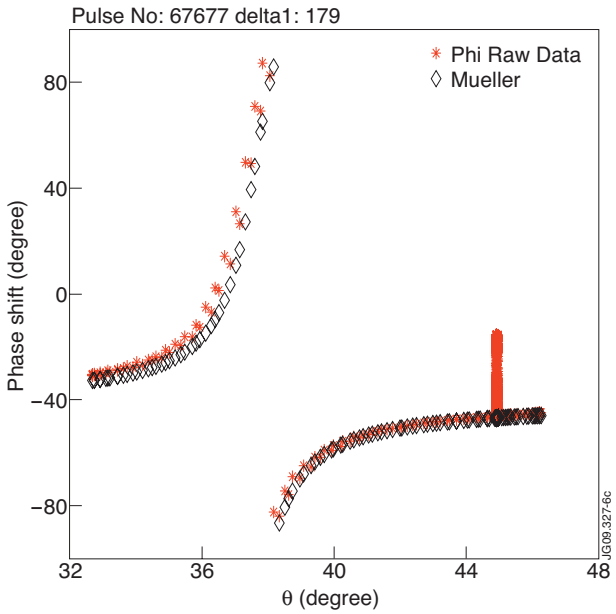

Figure 6: Comparison between the experimental calibration curve (asterisk) and the estimate of the new calibration model (diamond). Pulse No: 67677 chord #3

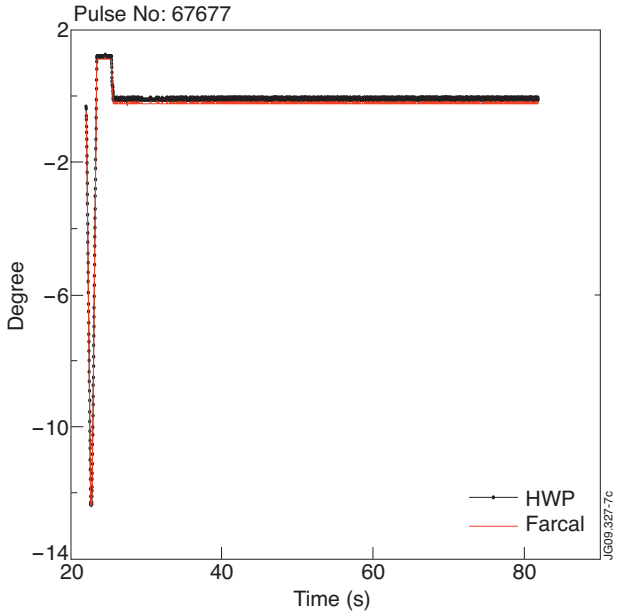

Figure 7: Calibration curve of Faraday angle (Pulse No: 67677 chord #3). Comparison between the experimental calibration curve (dot-line) and the estimate of the new calibration model (line).

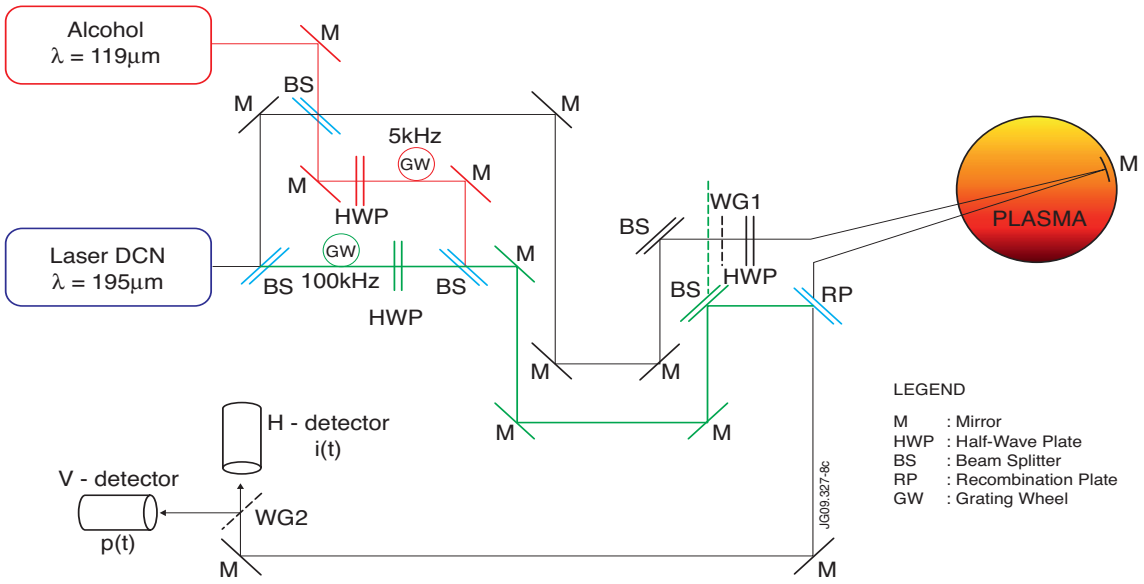

Figure 8: Schematic of the Polarimeter horizontal chords.

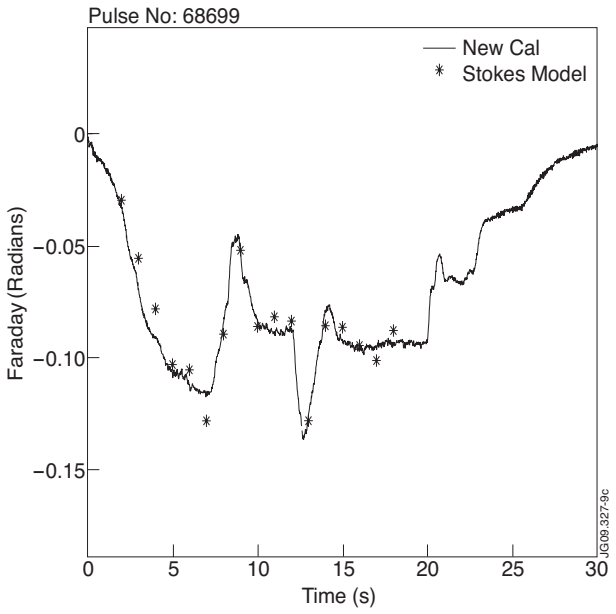

Figure 9: Comparison Faraday angle: new calibration (line) and numerical model (asterisk). Chord #2.

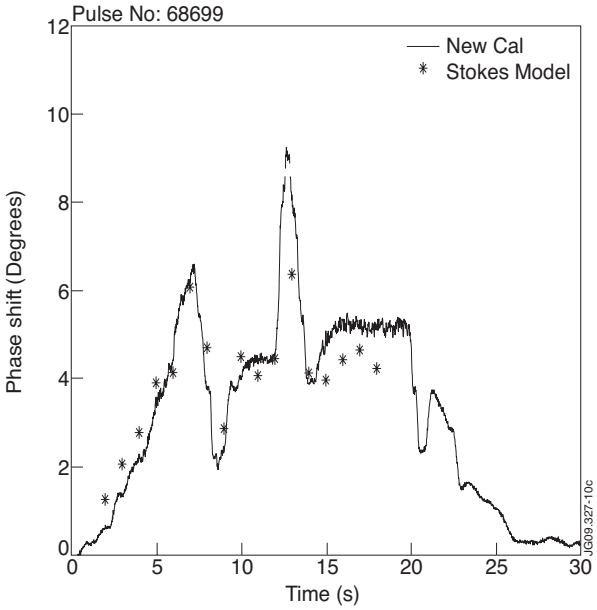

Figure 10: Phase shift: comparison between the new calibration (line) and numerical solution (asterisk). Chord #2

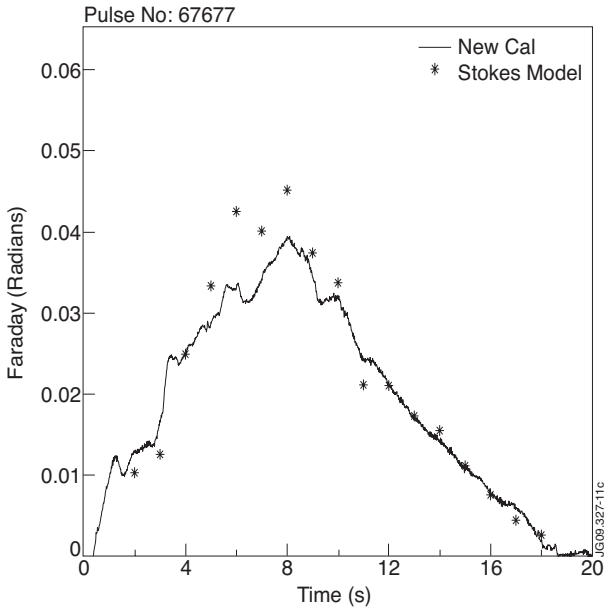

Figure 11: Comparison Faraday angle: new calibration (line) and numerical model (asterisk). Chord #3.

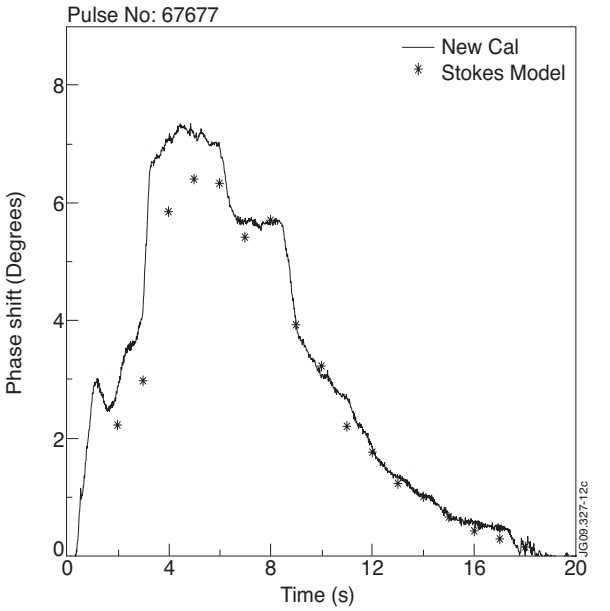

Figure 12: Phase shift: comparison between the new calibration (line) and numerical solution (asterisk). Chord #3.

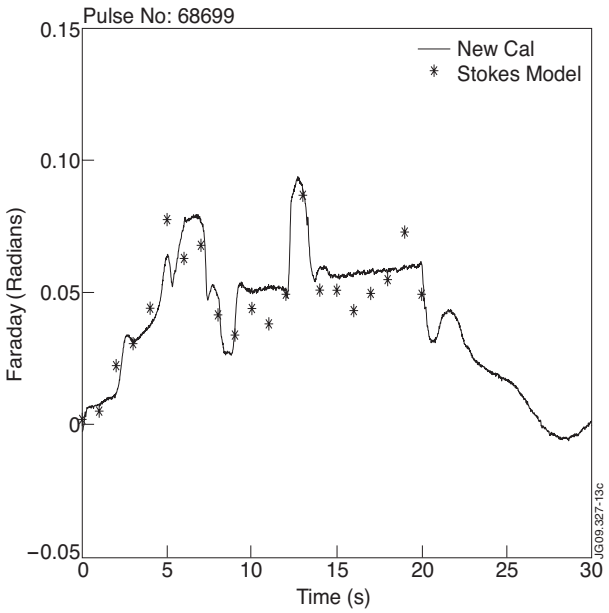

Figure 13: Comparison Faraday angle: new calibration (line) and numerical model (asterisk). Chord #4.

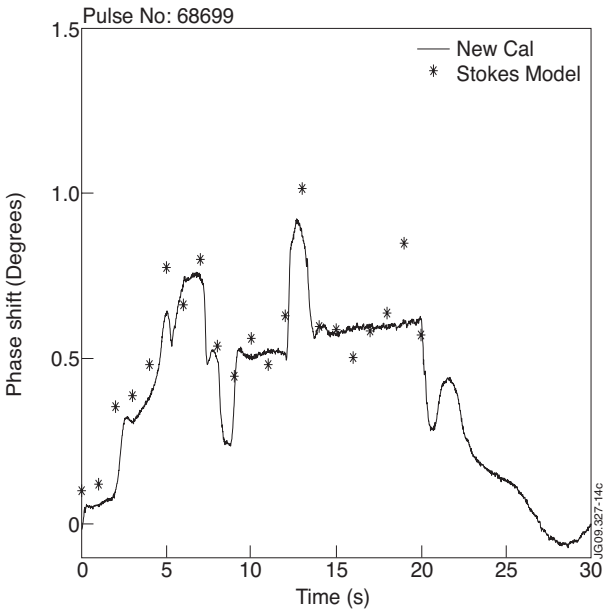

Figure 14: hase shift: comparison between the new calibration (line) and numerical solution (asterisk). Chord #4.

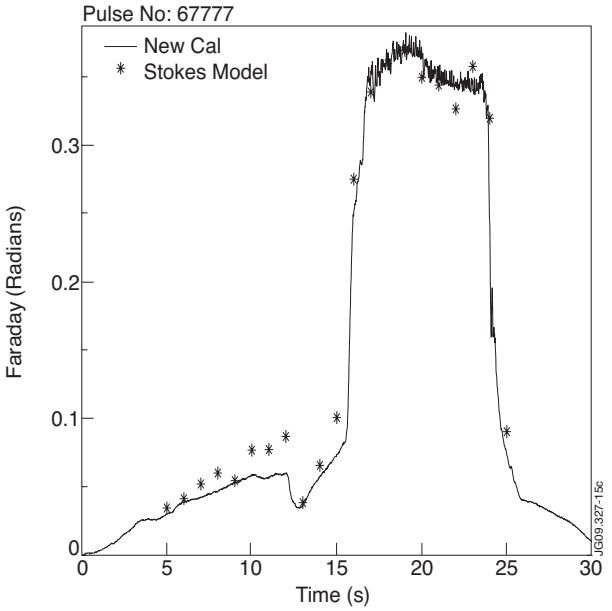

Figure 15: Comparison Faraday angle: new calibration (line) and numerical model (asterisk). Pulse No: 67777 chord #5.

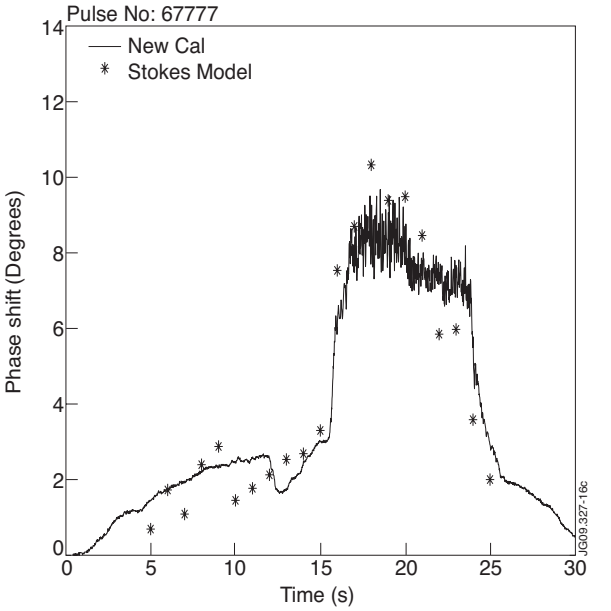

Figure 16: Phase shift: comparison between the new calibration (line) and numerical model (asterisk). Pulse No: 67777 chord #5.

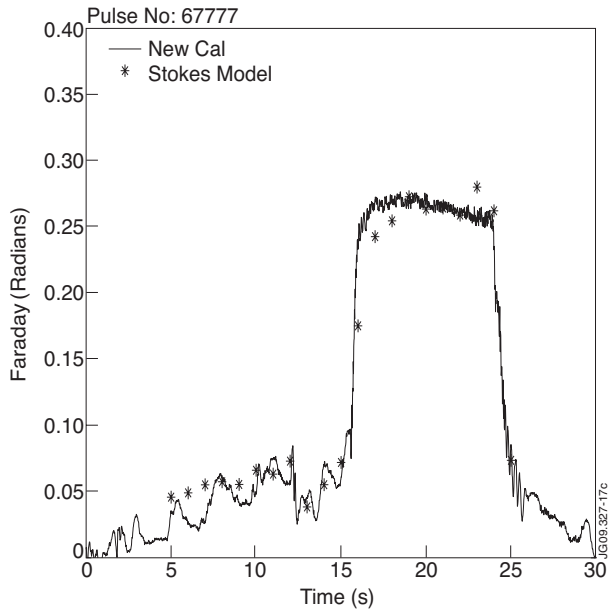

Figure 17: Comparison Faraday angle: new calibration (line) and numerical model (asterisk). Pulse No: 67777 chord #6.

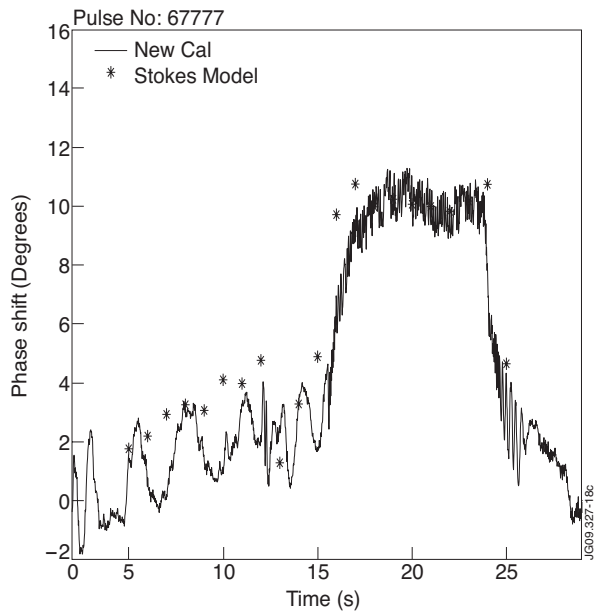

Figure 18: Phase shift: comparison between the new calibration (line) and numerical model (asterisk). Pulse No: 67777 chord #6.

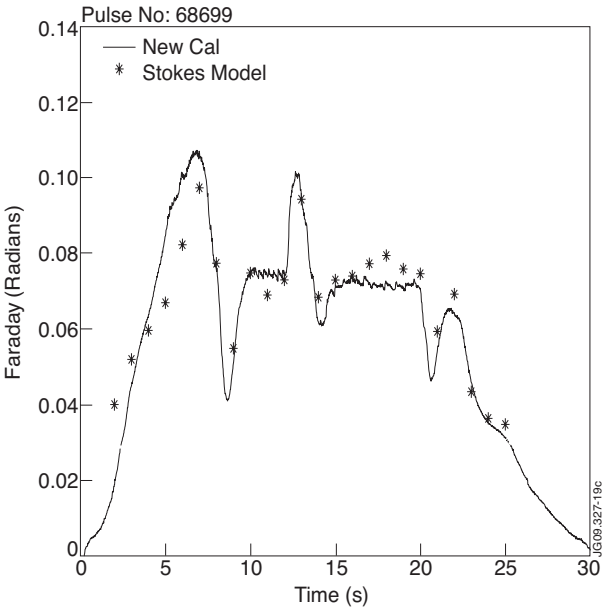

Figure 19: Comparison Faraday angle: new calibration (line) and numerical model (asterisk). Pulse No: 68699 chord #7.

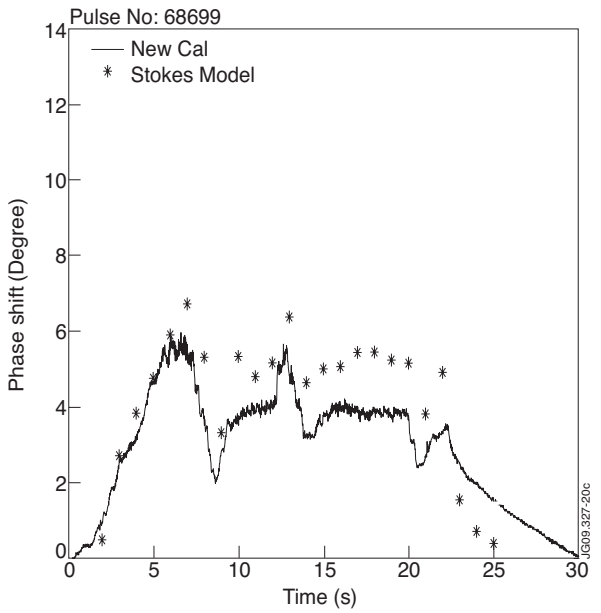

Figure 20: Phase shift: comparison between the new calibration (line), and numerical model (asterisk). Pulse No: 68699 chord #7.

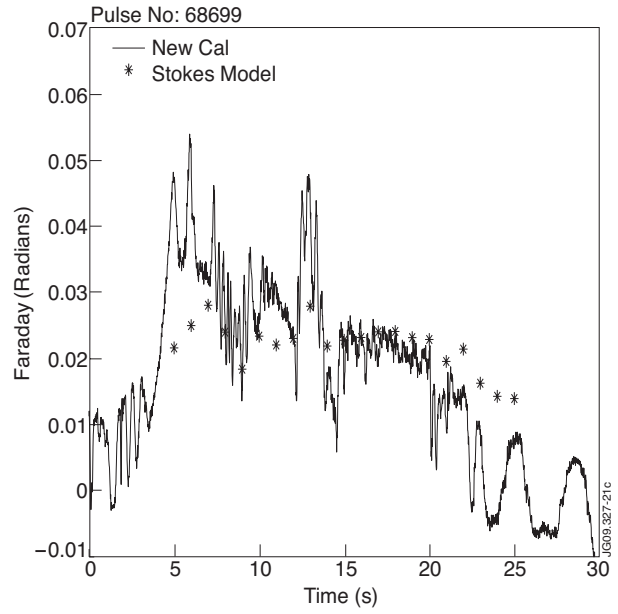

Figure 21: Comparison Faraday angle: new calibration (line) and numerical model (asterisk). Pulse No: 68699 chord #8.

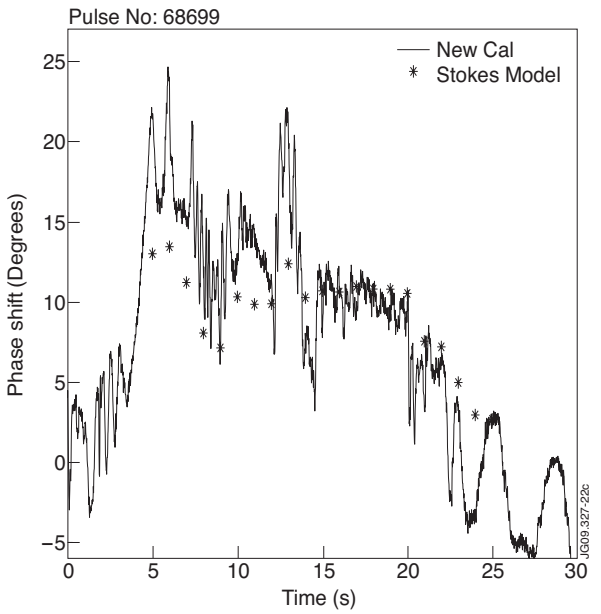

Figure 22: Phase shift: comparison between the new calibration (line) and numerical model (asterisk). Pulse No: 68699 chord #8.

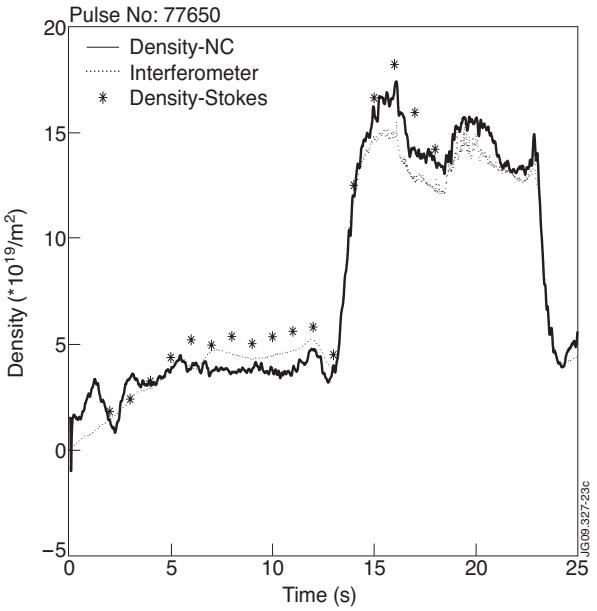

Figure 23: Comparison between the density with the new calibration (line) with the interferometer (dot line) and with the numerical solution (asterisk). Pulse No: 77650 chord #2.

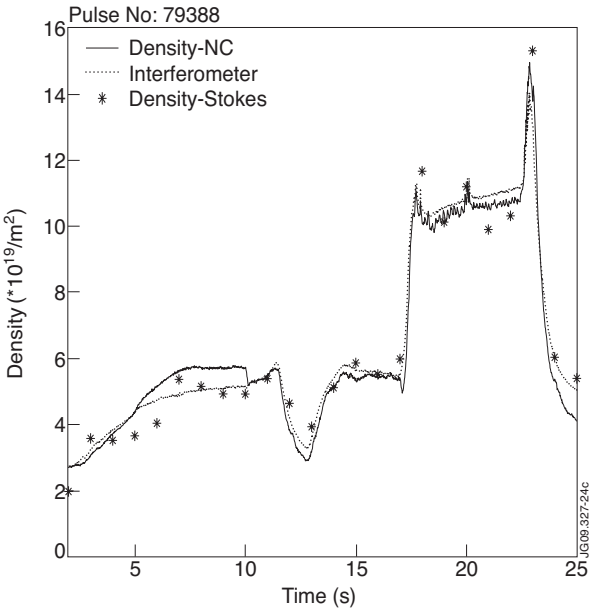

Figure 24: Comparison between the density with the new calibration (line) with the interferometer (dot line) and with the numerical solution (asterisk). Pulse No: 79388 chord #3.

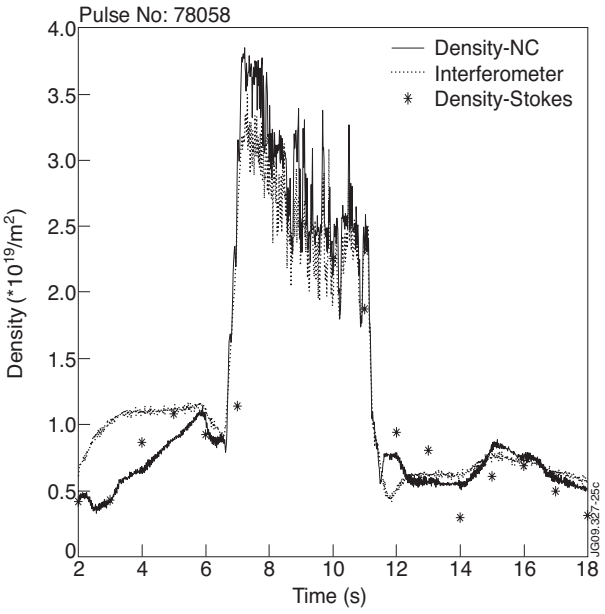

Figure 25: Comparison between the density with the new calibration (line) with the interferometer (dot line) and with the numerical solution (asterisk). Pulse No: 78058 chord #4.